Nanoscale

PAPER

View Article Online
View Journal | View Issue

Cite this: *Nanoscale*, 2024, **16**, 13895

Conductivity-mediated *in situ* electrochemical reconstruction of CuO_x for nitrate reduction to ammonia†

Hao Liang,‡[a] Yinqiao Zhang,‡[a] Xiaona Zhang,[a] Erzhuo Zhao,[c] Wendan Xue,[d] Enguang Nie,[e] Jianqiu Chen,*[a] Sijin Zuo*[a] and Minghua Zhou[b]

The electrocatalytic nitrate reduction reaction (NO_3RR) is an ideal NH_3 synthesis route with ease of operation, high energy efficiency, and low environmental detriment. Electrocatalytic cathodes play a dominant role in the NO_3RR. Herein, we constructed a carbon fiber paper-supported CuO_x nanoarray catalyst (CP/CuO_x) by an *in situ* electrochemical reconstruction method for NO_3^--to-NH_3 conversion. A series of characterization techniques, such as X-ray diffraction (XRD) and *in situ* Raman spectroscopy, unveil that CP/CuO_x is a polycrystalline-faceted composite copper nanocatalyst with a valence composition containing Cu^0, Cu^+ and Cu^{2+}. CP/CuO_x shows more efficient NO_3^--to-NH_3 conversion than CP/Cu and CP/Cu_2O, which indicates that the coexistence of various Cu valence states could play a dominant role. CP/CuO_x with a suitable Cu^{2+} content obtained by adjusting the conductivity during the *in situ* electrochemical reconstruction process exhibited more than 90% faradaic efficiencies for the NO_3RR in a broad range of −0.3 to −1.0 V *vs.* RHE, 28.65 mg cm^{-2} h^{-1} peak ammonia yield, and stable NO_3RR efficiencies for ten cycles. These findings suggest that CP/CuO_x with suitable copper valence states obtained by fine-tuning the conductivity of the electrochemical reconstruction may provide a competitive cathode catalyst for achieving excellent activity and selectivity of NO_3^--to-NH_3 conversion.

Received 13th April 2024,
Accepted 4th June 2024

DOI: 10.1039/d4nr01625d

rsc.li/nanoscale

1. Introduction

Ammonia (NH_3), as the essential chemical feedstock of pharmaceutical manufacturing, fertilizer production, energy supply, *etc.*, plays an important role in global energy and agricultural production.[1,2] At present, industrial-scale NH_3 synthesis is dominated by the energy-intensive Haber–Bosch (H–B) process. However, the H–B process requires high temperature (400–500 °C) and high pressure (150–300 atm), leading to the consumption of 2% of the world's annual energy output and 400 Mt of carbon dioxide emission per year.[3] Therefore, finding a new method for NH_3 synthesis that is environmentally friendly, efficient, and can utilize renewable energy sources has important research value and application prospects.

Electrocatalytic technologies are beginning to show their potential in NH_3 synthesis due to their ease of operation, high energy efficiency, and low environmental detriment.[4–6] The electrocatalytic nitrate reduction reaction (NO_3RR) is an ideal NH_3 synthesis route, which not only complements the traditional energy-intensive and costly NH_3 production process, but also helps to alleviate the environmental problems caused by nitrate pollution (such as eutrophication).[7–10] Nitrate reduced to ammonia would undergo a multi-step electroreduction process at the cathode that involves the transfer of nine protons and eight electrons to ultimately produce NH_3 and H_2O in acidic and neutral electrolytes.[11,12] Throughout the electrochemical reaction at the cathode, the rate-determining step ($*NH_3$ to NH_3) and the competing hydrogen evolution reaction (HER) dominantly impede the kinetics and faradaic efficiency of the NO_3RR.[13–16] As a result, it is crucial to rationally design cathode catalysts to achieve excellent activity and selectivity of the NO_3RR.

Various catalysts, including noble and transition metals, alloys, and non-metallic electrodes, have been explored to

[a]*State of Key Laboratory of Natural Medicines, School of Engineering, China Pharmaceutical University, Nanjing 210009, PR China. E-mail: sjzuo@cpu.edu.cn, cjqer@163.com*
[b]*Key Laboratory of Pollution Process and Environmental Criteria, Ministry of Education, College of Environmental Science and Engineering, Nankai University, Tianjin 300350, PR China*
[c]*School of Environment, Tsinghua University, Beijing 100084, PR China*
[d]*Department of Chemistry, Tsinghua University, Beijing 100084, PR China*
[e]*College of Bioscience and Biotechnology, Yangzhou University, Yangzhou, 225009, PR China*

†Electronic supplementary information (ESI) available. See DOI: https://doi.org/10.1039/d4nr01625d

‡These authors contributed equally to this work.

enhance the selectivity and efficiency of the NO_3RR.[17,18] For example, Liu *et al.* developed atomically precise silver (Ag) nanocluster catalysts for an efficient NO_3RR to synthesize NH_3, achieving high stability in neutral media.[19] A transition metal-based $Ni/Ni(OH)_2$ catalyst was reported to enable ammonia production at ampere-level current densities. Metal-free amorphous graphene was also found to benefit the direct electroreduction of nitrates to ammonia.[20] However, common issues with these catalysts include their limited availability, high cost, and potential deactivation over long-term use. Copper (Cu), on the other hand, shows promise in addressing these issues due to its abundance, lower cost, and superior NO_3^- adsorption and reduction of $*NO_3$ to $*NO_2$, which is attributed to the highly occupied d-orbitals and the energy level of Cu matching the lowest unoccupied $*\pi$ orbital of NO_3-N.[21] Nevertheless, pure Cu would rapidly deactivate owing to the NO_3RR intermediates (*e.g.*, NO_2^-) accumulating on the Cu surface.[22] To overcome this limitation, researchers have proved that optimizing the valence state of Cu is a preferable way, as $Cu^{\delta+}$ species (*e.g.*, CuO_x) with a relatively low energy barrier for the NO_3RR are more active in adsorbing, activating, and even desorbing the intermediates.[23–25] For instance, Wu *et al.* reported a strategy for controlling the oxidation state of copper using aryl diazonium salts for covalently binding aryl groups onto the copper surface.[26]

In this study, a carbon fiber paper-supported CuO_x nanoarray catalyst (CP/CuO_x) obtained by an *in situ* electrochemical reconstruction method was used for NO_3^--to-NH_3 conversion. The crystalline state, morphology, and electronic state of Cu were investigated by various spectroscopy characterization techniques. The performance of the CP/CuO_x cathode was assessed in the electrocatalytic reduction of NO_3^- to NH_3 including NH_3 yield, faradaic efficiency and stability. The electrochemical measurements, density functional theory (DFT) calculations, and spectroscopy characterization studies of CP/Cu, CP/Cu_2O and CP/CuO_x cathodes were compared to evaluate the role of CuO_x in NO_3^--to-NH_3 conversion. Finally, the effects of different physicochemical morphologies of CP/CuO_x constructed by conductivity modulation on NH_3 yield and faradaic efficiency were investigated.

2. Materials and methods

2.1 Working electrode preparation

The CP/Cu precursor was first synthesized using a chronoamperometry (i–t) method. As shown in Scheme 1, a carbon fiber paper sheet was used as the cathode (1 cm × 2 cm), a platinum sheet was used as the anode, and a saturated calomel electrode (SCE) was used as the reference electrode, respectively. 25 mL of electrolyte containing 70 mM $CuSO_4$ and 0.50 M Na_2SO_4 solution was added to a single-cell reactor. Then copper ions can be electrochemically reduced to metallic copper and deposited onto the carbon fiber paper at a constant stirring rate of 600 rpm and a deposition potential of 0.3 V *vs.* RHE for a duration of 800 seconds.

The acquired CP/Cu precursor was immersed in an alkaline solution which consisted of 2.5 M NaOH and 0.125 M $(NH_4)_2S_2O_8$ for 15 min to convert Cu to $Cu(OH)_2$. After washing 3–5 times with deionized water, the $Cu(OH)_2$ was dried. The $Cu(OH)_2$ was then pyrolyzed to obtain Cu_2O-loaded CP (CP/Cu_2O) at 550 °C for 2 hours in a tube furnace (inert gas atmosphere).

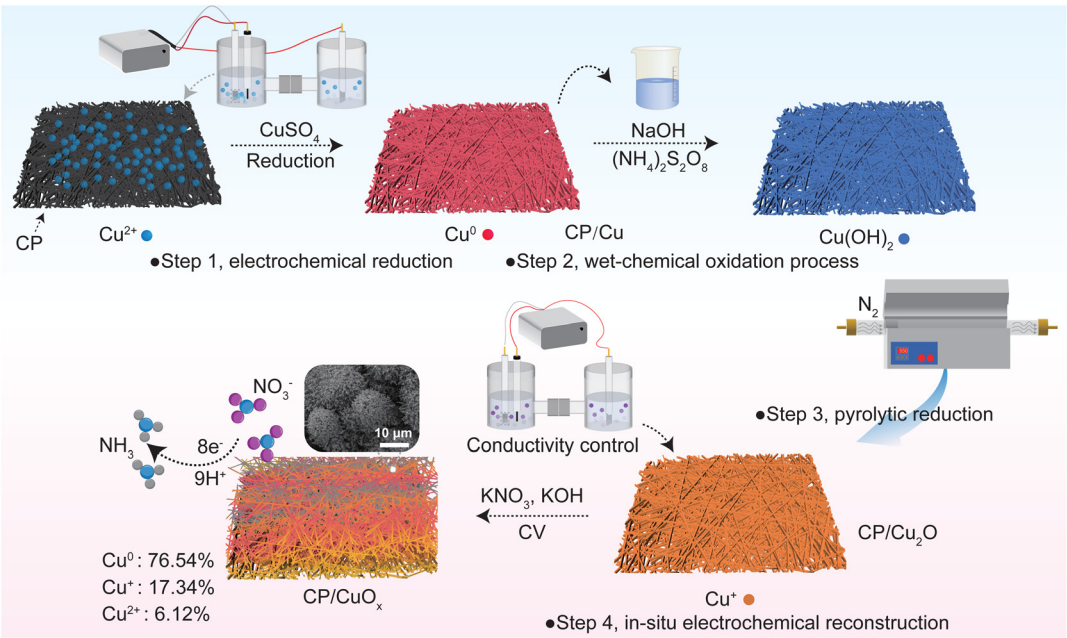

Scheme 1 Schematic illustration of the synthesis of CP/CuO_x.

CP/Cu_2O was treated by cyclic voltammetry (CV) for 50 electrolysis cycles (−0.5 to 0.2 V *vs.* RHE) in the alkaline electrolyte (1 M KOH) with varying nitrate concentrations, as displayed in Scheme 1. The nitrate concentrations of the alkaline electrolyte used were 0.1, 0.5, 0.8, and 1 M, and the corresponding conductivities of the electrolytes were 112, 128, 138, and 143 μS cm^{-1}, respectively.

2.2 Ammonia electrosynthesis

Electrochemical measurements were performed in an H-cell configured with the anodic and cathodic chambers (100 mL each) being separated by an anion exchange membrane (Nafion 115). 60 mL of 1 M KOH containing 0.1 M KNO_3 was added to each chamber. CP/CuO_x was used as the working electrode. Electrochemical methods including CV, linear scanning voltammetry (LSV), and electrochemical impedance spectroscopy (EIS) were used for characterization of the NO_3RR performance of the CP/CuO_x catalysts. LSV tests were performed in the range of −1 to 1 V *vs.* RHE at 5 mV s^{-1}. CV curves were recorded in the range of −0.52 to −0.62 V *vs.* RHE at 20, 40, 60, 80, 100, and 120 mV s^{-1} in 1 M KOH. EIS was conducted at 0.15 V *vs.* RHE and frequencies from 0.1 to 100 kHz. The measurement methods of NO_2^-, NO_3^-, NH_4^+, N_2H_4, N_2 and H_2 are depicted in the ESI,† and their standard curves are shown in ESI Fig. S1–S5.†

3. Results and discussion

3.1 Preparation and characterization of electrodes

The preparation process of the CP/CuO_x electrode is shown in Scheme 1. First, the CP was pre-treated to remove the impurities on the fiber surface and to improve the attachment point of the copper grains. CP loaded with copper grains (CP/Cu) was obtained by chronoamperometry, and the optimum copper deposition state was obtained by tuning the deposition potential and reaction time (ESI Fig. S6 and S7†). The copper grains on CP/Cu were converted to $Cu(OH)_2$ by wet chemistry. They were then annealed to obtain CP/Cu_2O by the thermal decomposition method. Finally, CP/Cu_2O was reduced to a composite Cu nanocatalyst (CP/CuO_x) with better electrochemical stability in solutions containing nitrates. During the *in situ* electrochemical reconstruction process, the CV curves of the first 40 cycles varied significantly and with little overlap, indicating that Cu_2O was reduced on the surface of the carbon fibers (ESI Fig. S8a and b†). In subsequent cycles, the CV curves show good overlap, demonstrating that the catalyst has formed a stable chemical state (ESI Fig. S8c and d†).

As shown in Fig. 1a and b, after the *in situ* electrochemical reconstruction process, CP/CuO_x formed a cluster-like structure consisting of many spherical nanograins on its surface at a conductivity of 112 μS cm^{-1}. The characteristic diffraction peaks of C, Cu and Cu_2O are observed in the XRD spectra of the CP/CuO_x electrocatalyst, as shown in Fig. 1c and ESI Table S1.† The diffraction peaks of C are from the graphitic carbon structure of the CP, with 26.5° being attributed to the (002) facet and 54.5° being attributed to the (004) plane of the carbon substrate.[27] The weaker diffraction peaks observed at 43.3° and 50.5° are attributed to the Cu (100) facet and the Cu (111) plane, respectively. It is important to note that the (200) diffraction peak is a secondary diffraction originating from the (100) plane.[28,29] The CP/CuO_x electrocatalyst showed weakly (100)- and (111)-oriented CuO crystalline phases and also strongly (100)-, (111)-, and (220)-oriented Cu_2O crystalline phases. The elemental composition and valence states of CP/CuO_x were further investigated by XPS. One can see in Fig. 1d that CP/CuO_x exhibits the characteristic peaks of C 1s, O 1s, Cu LMM, Cu 2p3/2 and Cu 2p1/2.[30,31] As displayed in Fig. 1e, there are three different types of oxygens present in CP/CuO_x, namely O_I (oxygen on the complex structure), O_{II} (oxygen on the Cu/Cu_2O structure) and O_{III} (oxygen-deficient species).[32–35] This also indicates that CP/CuO_x is a mixed-valence copper nanocatalyst. Fig. 1f shows the high-resolution Cu LMM XPS spectrum of CP/CuO_x. The three peaks observed at 567.76, 573.94 and 571.80 eV correspond to Cu^0 (76.54%), Cu^+ (17.34%) and Cu^{2+} (6.12%), respectively.[36–38] In addition, our Cu 2p XPS spectrum (ESI Fig. S9†) also showed a similar phenomenon of mixed Cu^{2+} and Cu^+/Cu^0. These results collectively demonstrated that CP/CuO_x is a polycrystalline-faceted composite copper nanocatalyst.

3.2 Evaluation of ammonia electrosynthesis

The catalytic activity of CP/Cu, CP/Cu_2O and CP/CuO_x for the electroreduction of nitrate to ammonia was investigated in H-cells. Before investigating the NO_3RR performance of the catalysts, their LSV curves were tested until the polarization curves reached a steady state. Fig. 2a shows the LSV curves of the three catalysts. In general, the presence of NO_3^- leads to an increase of current density for the three catalysts. The phenomenon indicates that the NO_3^- reduction process occurred on the three catalysts.[39,40] Moreover, the current density of CP/CuO_x with NO_3^- shows the most significant increase compared to that of virgin CP, CP/Cu and CP/Cu_2O (Fig. 2a and ESI Fig. S10†). In particular, at −0.4 V *vs.* RHE, the current density of CP/CuO_x increased to −311 mA cm^{-2}, which is approximately 2.78 times higher than that of CP/Cu. The results suggest that more NO_3^- reduction occurred on the CP/CuO_x cathode.

In addition, we further investigated the kinetics of the NO_3RR by analyzing the Tafel curves of the three catalysts (Fig. 2b). CP/CuO_x exhibited the smallest Tafel slope (194.09 mV dec^{-1}) compared to CP/Cu (255.06 mV dec^{-1}) and CP/Cu_2O (233.55 mV dec^{-1}), suggesting that the composite state Cu interface of CP/CuO_x is beneficial for improving the reaction kinetics compared to pure Cu. The higher electrochemically active surface area (ECSA) and the electrochemical double-layer capacitance (C_{dl}) values of CP/CuO_x than those of CP/Cu and CP/Cu_2O (Fig. 2c and ESI Fig. S11†) indicate more catalytically active sites on CP/CuO_x. Furthermore, EIS measurement was also used to further confirm the excellent electrocatalytic performance of CP/CuO_x. The Nyquist plots of EIS show that CP/CuO_x exhibited a lower charge transfer impe-

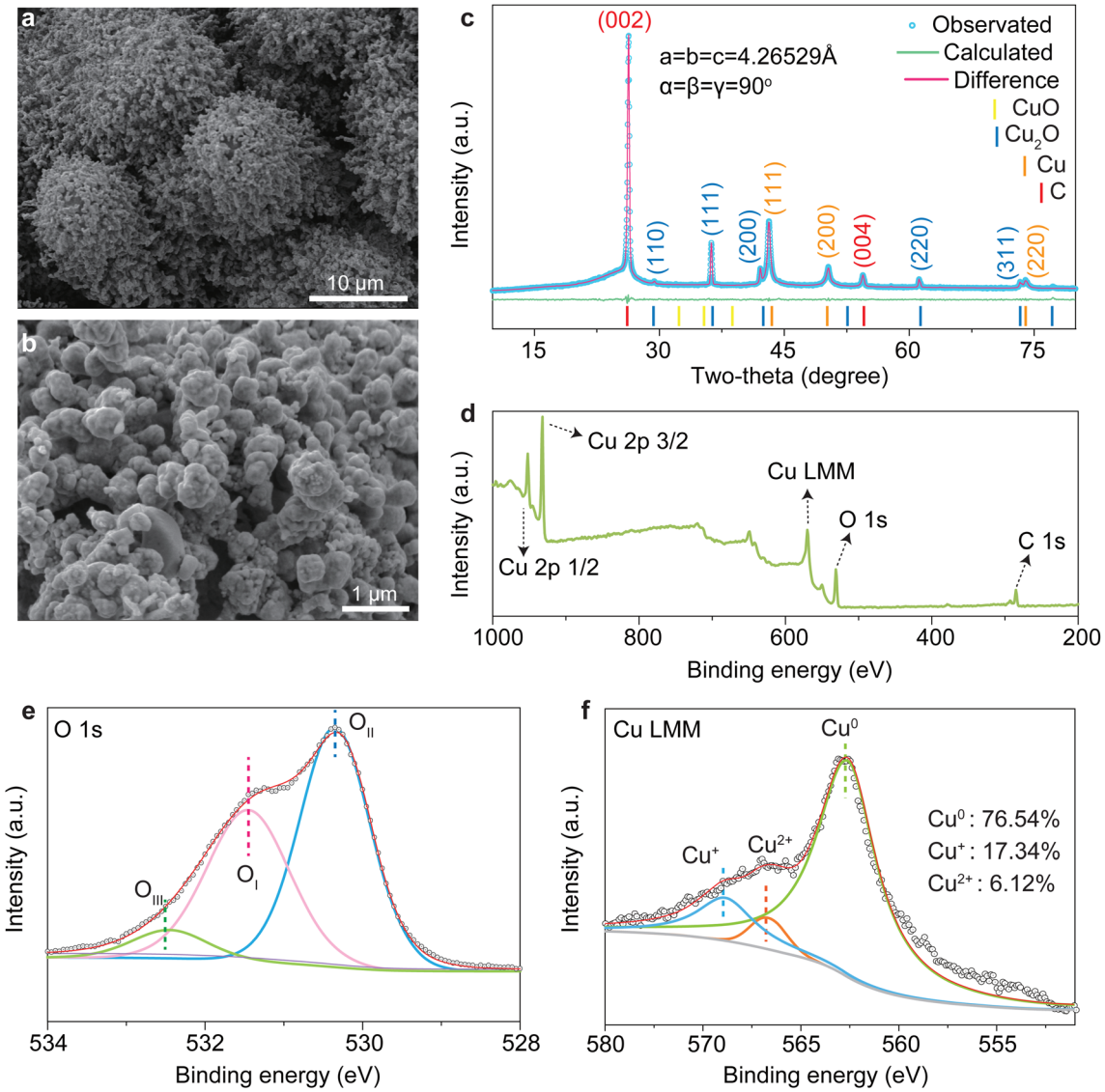

Fig. 1 Characterization of CP/CuO_x. (a and b) SEM images of CP/CuO_x. (c) XRD patterns of CP/CuO_x (Cu_2O: JCPDF No. 05-0667; CuO: JCPDF No. 48-1548; Cu: JCPDF No. 04-0836; C: JCPDF No. 23-0064). (d) XPS survey spectrum of CP/CuO_x. (e) High-resolution O 1s XPS spectrum and (f) high-resolution Cu LMM XPS spectrum of CP/CuO_x.

dance than the control groups, implying a more efficient electron transfer on the surface of CP/CuO_x (Fig. 2d).

In the electrolysis experiments after 8 h, the CP/CuO_x electrocatalyst was able to promote the conversion of NO_3^- to NH_4^+ consistently and efficiently, with the intermediate product NO_2^- almost not accumulating but being rapidly converted (Fig. 2e). In order to gain insight into the reduction of NO_3^- to NH_3 over CP/CuO_x in a mixed solution of 0.1 M KNO_3 and 1 M KOH, electrochemical *in situ* Raman spectroscopy measurements were performed at −0.6 V *vs.* RHE for a duration of 1 h. As shown in Fig. 2f, CP/CuO_x shows peaks stretching at 730 and 1047 cm^{-1}, which were attributed to the vibrational modes of N–O (NO_3^-) and free NO_3^- in the liquid environment.[41,42] The stretching intensity of these peaks increased gradually as the reaction time extended from 0 to 60 min, indicating the aggregation of NO_3^- on the catalyst due probably to the strong adsorption of NO_3^- on the CP/CuO_x surface. The vibrational peaks at 1280 and 1548 cm^{-1} are attributed to the reaction intermediates of $*NO_2$ and *HON, and the Raman signals of these intermediates are weak during the reaction (ESI Fig. S12†).[43,44] Nevertheless, the Raman peak at 1664 cm^{-1} attributed to NH_2 is clearly stronger.[45] These phenomena indicated that the NO_3RR could rapidly convert to ammonia accompanied by some detectable intermediates through a stepwise deoxygenated hydrogenation pathway on the CP/CuO_x cathode.

The efficient catalytic performance of CP/CuO_x in ammonia production from nitrate reduction can be attributed to the suitable valence of Cu. With respect to the detailed role of Cu in each specific valence state, we tentatively considered them

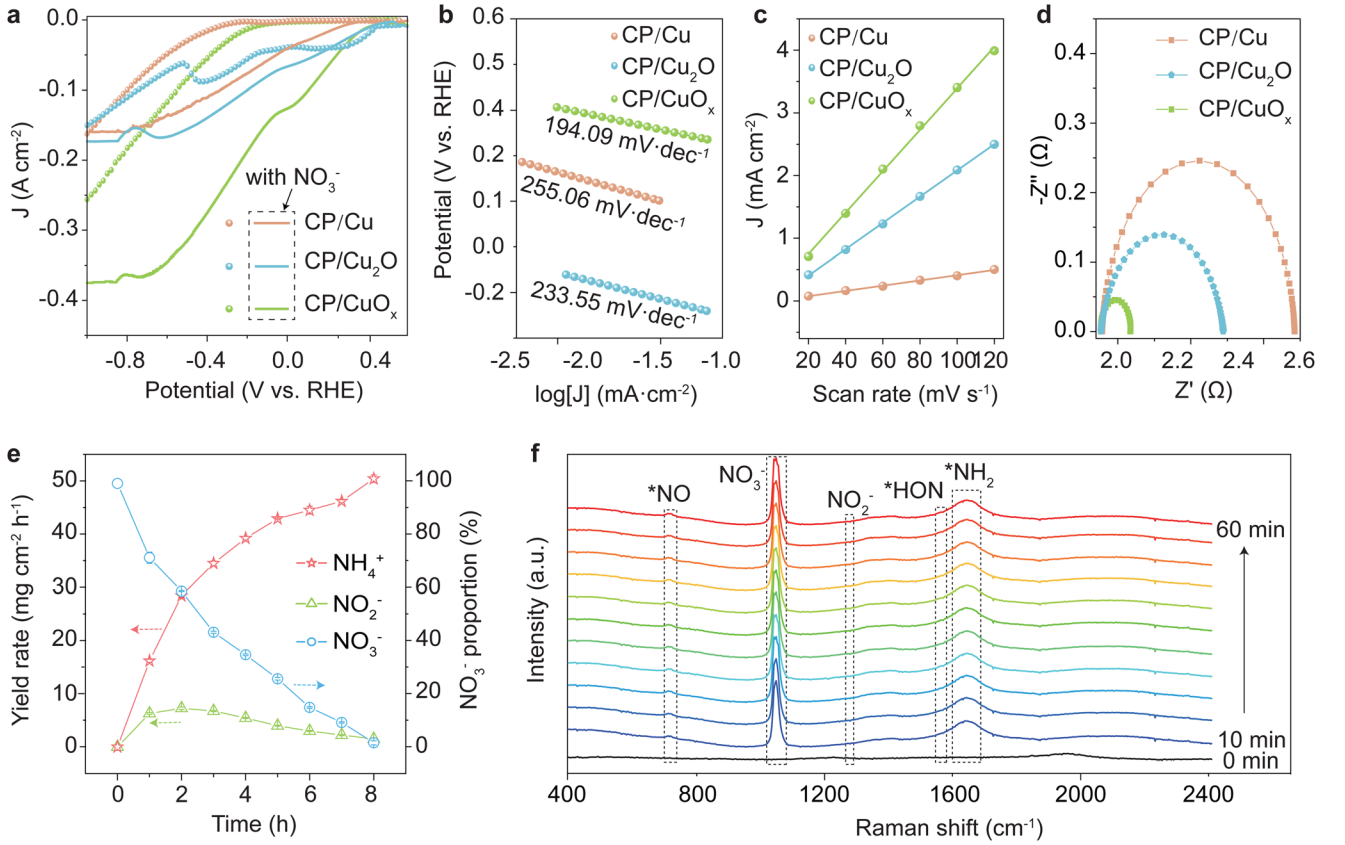

Fig. 2 Electrochemical performance of CP/CuO_x. (a) LSV curve of CP/CuO_x. (b) Tafel slope of nitrate reduction by CP/CuO_x. (c) C_{dl} of nitrate reduction for CP/CuO_x. (d) Nyquist plots of CP/CuO_x. (e) Eight hours of NO_3RR reaction process. 1 M KOH solution containing 0.1 M NO_3^- as the electrolyte. (f) *In situ* Raman spectra of CP/CuO_x during its electrochemical process.

from the viewpoint of Gibbs free energy of reaction intermediates (ESI Fig. S13†) by DFT calculations. The calculated results indicate that Cu^0 has a positive contribution to the conversion of NO_3^- to $*NH_3$ but a thermodynamically unfavorable process is the desorption of $*NH_3$. Cu^+ displays a favorable NO_3^- adsorption ($*NO_3$) compared to Cu^0 and Cu^{2+} because of a higher downhill energy barrier of −4.02 eV, nevertheless only −1.88 and −1.84 eV on Cu^0 and Cu^{2+} respectively. Unfortunately, Cu^+ has the very difficult step in the conversion of "*NO to *N" owing to an uphill energy barrier of 1.74 eV. Regarding Cu^{2+}, it almost displays all beneficial steps in coordinate numbers of 1–8 from the conversion of "NO_3^- to $*NH_3$" aside from a slight uphill of 1.24 eV (*versus* 1.74 eV on Cu^+) in the foregoing step of "*NO to *N". Importantly, Cu^{2+} displays the smallest uphill energy barrier for the final desorption of the $*NH_3$ intermediate which serves as the rate-determining step for Cu^0, Cu^+ and Cu^{2+}. Therefore, the valence composition of Cu plays a key role in our NO_3RR performance.

The performance of CP/CuO_x in ammonia synthesis at different potentials (−0.1 to −1.0 V *vs.* RHE) was deeply investigated. To verify that ammonia production originated from the electrochemical reduction of NO_3^- entirely, CP/CuO_x was placed in electrolyte with and without NO_3^- for electrocatalytic tests (please see 2.2 Ammonia electrosynthesis). As shown in ESI Fig. S14,† almost no ammonia generation was detected in the solution without NO_3^-, further confirming that the ammonia originated totally from the reduction of NO_3^-. The complementary ^{15}N isotopic labeling experiment showed a typical double peak with chemical shifts at 6.85 and 6.97 ppm in the ^1H NMR spectrum (ESI Fig. S15†), indicating the above similar conclusion. As shown in Fig. 3a and ESI Fig. S16a,† CP/CuO_x exhibited faradaic efficiencies of more than 90% in the range of −0.3 to −1.0 V *vs.* RHE and realized a peak ammonia yield of 28.65 mg cm^{-2} h^{-1} at a potential of −0.9 V *vs.* RHE. Such high selectivity to NH_3 was probably attributed to the suitable adsorption energy and a favorable thermodynamic process for some key intermediates over our electrocatalyst. Other by-products such as H_2 or N_2H_4 were not detectable in our system (ESI Fig. S4, S5 and S17†). However, the faradaic efficiency still not being equal to 100% was probably attributed to the detectable reaction-incomplete intermediate NO_2^- (Fig. 2e). CP/CuO_x performed well in terms of ammonia yield and faradaic efficiency, well in agreement with the results of their LSV, ECSA, and EIS tests. A suitable potential of −0.6 V *vs.* RHE was chosen to test the long-term stability of CP/CuO_x, as can be seen in Fig. 3b. The results show that there was almost no performance attenuation in the continuous ammonia electrosynthesis with the CP/CuO_x electrocatalyst

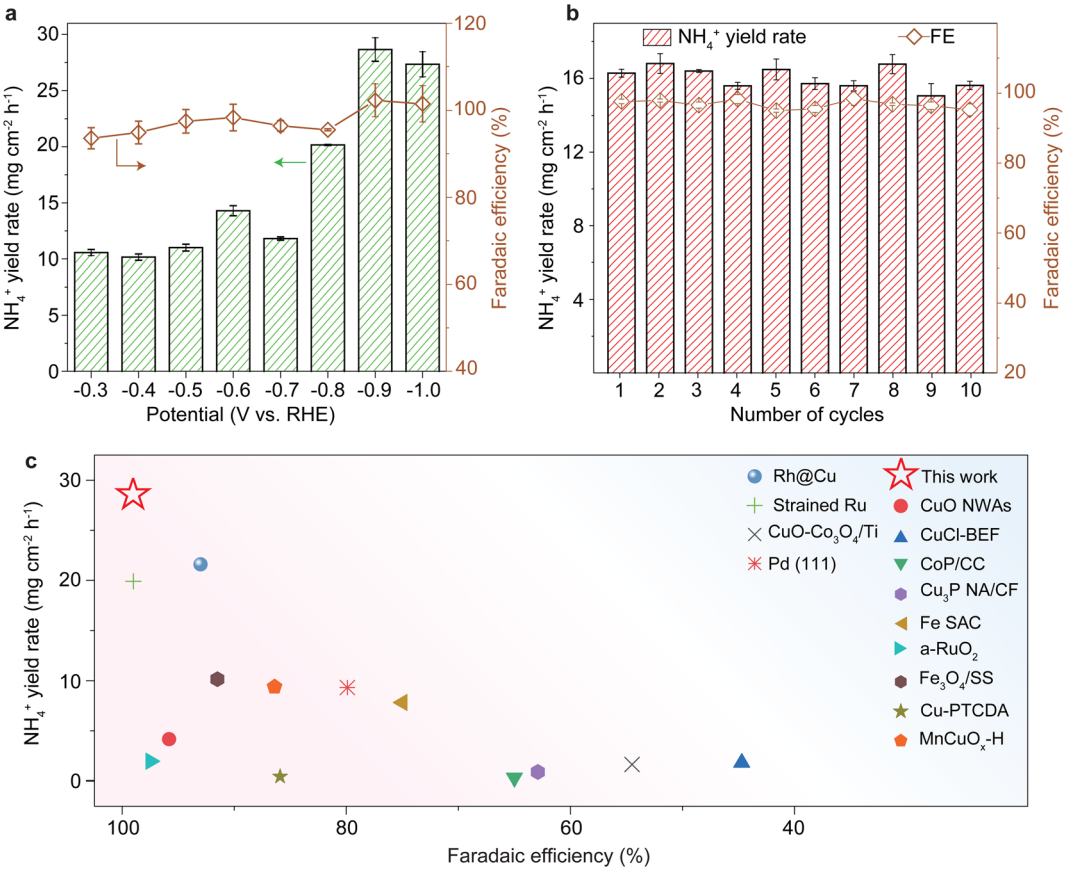

Fig. 3 Ammonia electrosynthesis performance. (a) Faradaic efficiencies and NH_4^+ yields at different step potentials of CP/CuO_x. (b) The as-obtained faradaic efficiency and NH_4^+ yield during the cycling stability test of CP/CuO_x. (c) Performance comparison of ammonia electrosynthesis and its faradaic efficiency in the NO_3RR between our work and the reported studies.

during 10 cycles. In addition, no significant changes were still observed in the CV curves (ESI Fig. S18†), Cu LMM XPS spectra (ESI Fig. S19a†) and Raman spectra (ESI Fig. S20†) of the catalysts before and after the reaction, and even the neglected Cu leaching (ESI Fig. S19b and c†) in each repeated run, together indicating that the catalyst composition remained robust even after ten cycle tests. Compared to the reported copper catalysts and other advanced catalysts, the CP/CuO_x electrocatalyst in this study showed superior faradaic efficiency and NH_4^+ yield for the NO_3RR (Fig. 3c and ESI Table S2†).

3.3 Unveiling of the role of conductivity in the reconstruction of CuO_x

To investigate the surface compositions and valence states of Cu for the NO_3RR, the CP/CuO_x, CP/CuO_{x+1}, CP/CuO_{x+2} and CP/CuO_{x+3} catalysts were prepared in 112, 128, 138 and 143 μS cm^{-1} electrolyte, respectively, through an *in situ* electrochemical reconstruction process (please see 2.1 Working electrode preparation). Note that the increased oxygen element indicates the increased valence of copper. With increasing the conductivity of electrolyte from 128 to 143 μS cm^{-1}, the morphologies of CP/$CuO_&$ ranged from a spherical-like cluster consisting of numerous rod-shaped copper grains (128 μS cm^{-1}, Fig. 4a) to irregularly distributed copper grains (138 μS cm^{-1}, Fig. 4b) and a more ordered distribution of large rod-like copper grains (143 μS cm^{-1}, Fig. 4c). Changes in the chemical compositions of these CP/$CuO_&$ electrocatalysts were first detected by Raman spectroscopy (Fig. 4d). The characteristic Raman peaks of Cu^+ and Cu^{2+} could be clearly observed, such as the stretching peak at about 300 cm^{-1} pointed to the CuO (Cu^{2+}) phase.[46] This result is consistent with the valence changes revealed by XPS, as shown in Fig. 4e. In the XPS spectra of CP/CuO_{x+1}, CP/CuO_{x+2} and CP/CuO_{x+3}, the signals of the Cu^{2+} species become more prominent with increasing conductivity. The results indicate that the four catalysts consist of Cu^0, Cu^+ and Cu^{2+} and that the amount of Cu^{2+} increases from 6.94% to 25.91% with increasing conductivity (ESI Table S3†). In addition, the XRD results in ESI Fig. S21† support a similar conclusion, with the intensity of the Cu (100), (111) and Cu (220) facets decreasing progressively as the conductivity of electrolyte increases, while the intensities of the diffraction peaks representing the CuO phase increase gradually.

The *in situ* electrochemical reconstruction by CV was found to be two stages of dissolution (oxidation process) and redeposition (reduction process) of copper ions.[47] The Cu^{2+} ions of the catalyst would leach into the electrolyte during the

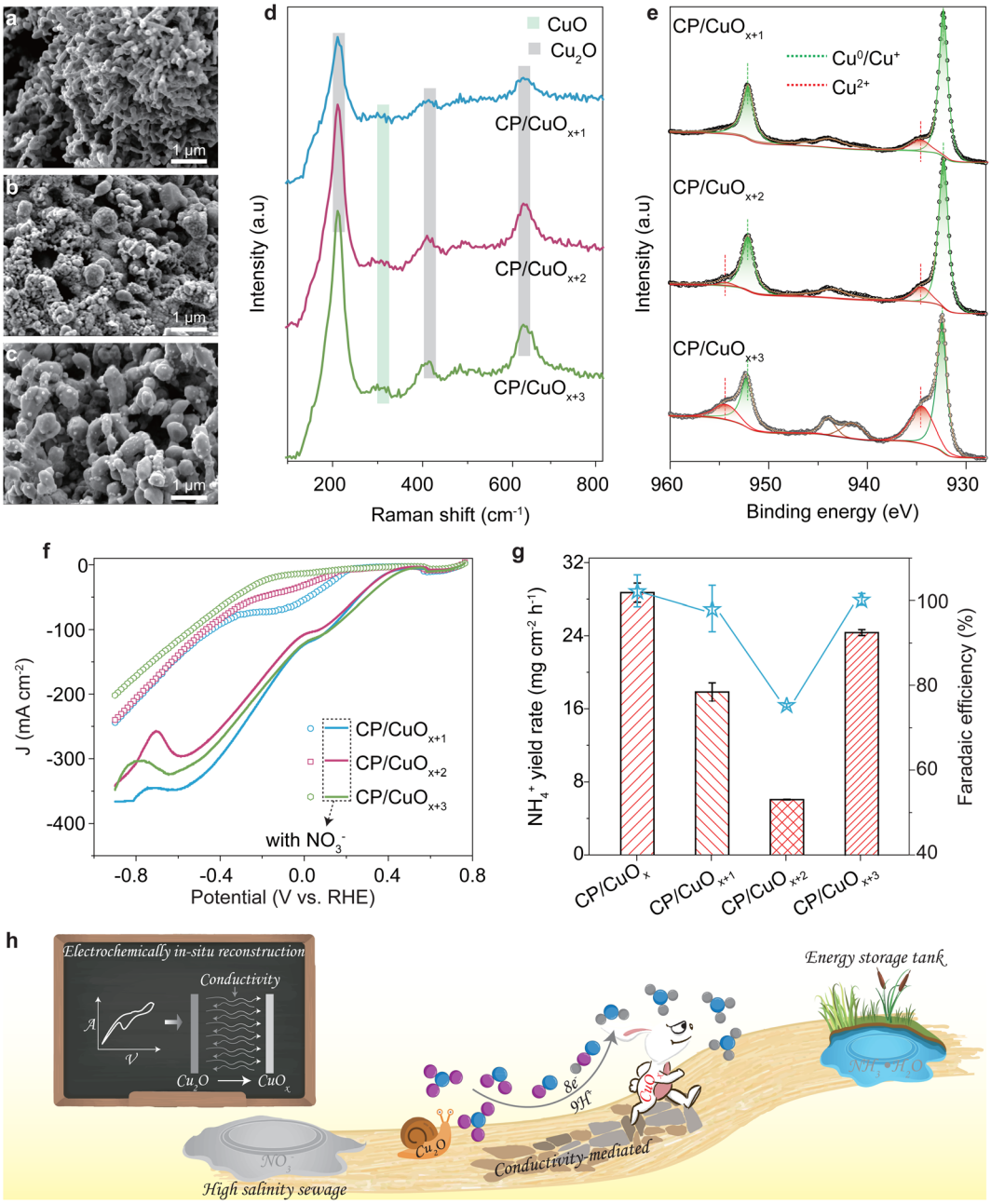

Fig. 4 Conductivity-mediated electrochemical reconstruction of CuO_x. (a–c) SEM images of CP/CuO_{x+1}, CP/CuO_{x+2} and CP/CuO_{x+3}. (d and e) Raman spectra and high-resolution Cu 2p XPS spectra of CP/CuO_{x+1}, CP/CuO_{x+2} and CP/CuO_{x+3}. (f) LSV curves of CP/CuO_{x+1}, CP/CuO_{x+2} and CP/CuO_{x+3}. (g) Faradaic efficiencies and NH_4^+ yields of CP/CuO_{x+1}, CP/CuO_{x+2} and CP/CuO_{x+3}. (h) Schematic illustration of the conductivity-mediated *in situ* electrochemical reconstruction of CuO_x for nitrate reduction to ammonia.

oxidation process, and then the Cu^+ or Cu^0 would redeposit onto the catalyst during the reduction process. A decrease in the conductivity of the electrolyte leads to an increase in electrical resistance, which slows down the ion migration rate in turn.[48] Consequently, in a low conductivity microenvironment, slow ion migration causes a higher accumulation of Cu^{2+} on the catalyst surface. This would contribute to the formation of a clustered deposit with some lower valence copper during the reduction process (ESI Fig. S22†). In contrast, at higher conductivity, Cu^{2+} ions can migrate and diffuse faster, resulting in a decrease in the local Cu^{2+} concentration in the electrolyte which would cause the slight reduction of Cu^{2+} on the catalyst ($Cu^{2+}{}_{liquid} \rightarrow Cu^0/Cu^+{}_{solid}$). Thus, we could obtain more Cu^{2+} on the catalyst in a higher conductivity microenvironment (Fig. 4e and ESI Table S3†).

LSV analysis shows the current responses of CP/CuO_{x+1}, CP/CuO_{x+2} and CP/CuO_{x+3} to NO_3^-, and the current densities vary, in the sequence of CP/CuO_{x+3} > CP/CuO_{x+1} > CP/CuO_{x+2}

(Fig. 4f). This order is accordingly consistent with their ammonia yields and faradaic efficiency (Fig. 4g and ESI Fig. S16†). In terms of NO_3RR performance, CP/CuO_x produced with the lowest conductivity performs best, followed by CP/CuO_{x+3} with the highest conductivity. The Raman spectrum of CP/CuO_{x+3} was similar to that of CP/CuO_x after 1 or 10 electrolysis experiments (ESI Fig. S20c†). The phenomenon indicates that CP/CuO_{x+3} is unstable during electrolysis, and this would lead to a shift towards a similar chemical composition to CP/CuO_x, even for the initial CP/CuO_{x+3} electrocatalyst with the highest Cu^{2+} content. As a result, the NO_3RR performance of CP/CuO_{x+3} was close to that of CP/CuO_x (Fig. 4g).

These results clearly indicate that conductivity-mediated *in situ* electrochemical reconstruction of CuO_x can not only tune the physicochemical characteristics of catalysts, such as the physical morphology (Fig. 4a–c), but also, importantly, effectively control the valence state of copper which plays a key role in the NO_3RR performance. The comparison of the NO_3RR performance of CP/CuO_x with that of CP/Cu_2O and CP/Cu in Fig. 2a shows that the catalysts with all three valence states (Cu^0, Cu^+ and Cu^{2+}) exhibit desirable nitrate reduction. Furthermore, the results in Fig. 3 and 4f, g proved the significance of a suitable content of Cu^{2+} in the CuO_x electrocatalyst. The phenomena could be attributed to the easy formation of some key reaction intermediates during the NO_3RR process and effective suppression of the competitive cathodic HER (see ESI Fig. S13 and S17†) on the CuO_x interface.[49,50] Therefore, for achieving a high NH_3 yield during the NO_3RR process, an appropriate conductivity microenvironment is needed to optimize the ratio of Cu valence states.

4. Conclusions

This study introduces a carbon fiber paper-supported CuO_x nanoarray catalyst (CP/CuO_x) obtained by an *in situ* electrochemical reconstruction method for NO_3^--to-NH_3 conversion. The CP/CuO_x catalyst with various valence states of Cu shows an obvious improvement in NO_3^--to-NH_3 conversion in comparison with CP/Cu and CP/Cu_2O. CP/CuO_x with a suitable Cu^{2+} content exhibited good stability, high faradaic efficiencies and high ammonia yields in a wide potential range. The results suggest that CP/CuO_x obtained by the conductivity-mediated *in situ* electrochemical reconstruction route may provide a commercially competitive electrocatalyst for achieving excellent activity and selectivity of NO_3^--to-NH_3 conversion (Fig. 4h).

Author contributions

Hao Liang: methodology, data curation, formal analysis, and writing – original draft. Yinqiao Zhang: visualization and writing – review and editing. Xiaona Zhang: methodology and visualization. Erzhuo Zhao: validation and formal analysis. Wendan Xue: supervision and formal analysis. Enguang Nie: formal analysis and writing – review and editing. Minghua Zhou: writing – review and editing. Jianqiu Chen: methodology. Sijin Zuo: conceptualization, supervision, project administration, and funding acquisition.

Conflicts of interest

There is no conflict of interest to declare.

Acknowledgements

We are thankful for the financial support of the National Natural Science Foundation of China (No. 22306202 and 22306201) and the Natural Science Foundation of Jiangsu Province (No. BK20231026).

References

1 K. Zhang, A. Cao, L. H. Wandall, J. Vernieres, J. Kibsgaard, J. K. Norskov and I. Chorkendorff, Spin-mediated promotion of Co catalysts for ammonia synthesis, *Science*, 2024, **383**, 1357–1363.
2 X. Zheng, J. C. Hao, Z. C. Zhuang, Q. Kang, X. F. Wang, S. L. Lu, F. Duan, M. L. Du and H. Zhu, Emerging electrospinning platform toward nanoparticle to single atom transformation for steering selectivity in ammonia synthesis, *Nanoscale*, 2024, **16**, 4047–4055.
3 S. T. Wang, Y. Liu, K. Zhang and S. Y. Gao, Self-powered electrocatalytic nitrate to ammonia driven by lightweight triboelectric nanogenerators for wind energy harvesting, *Nano Energy*, 2023, **112**, 108434.
4 S. Han, H. Li, T. Li, F. Chen, R. Yang, Y. Yu and B. Zhang, Ultralow overpotential nitrate reduction to ammonia via a three-step relay mechanism, *Nat. Catal.*, 2023, **6**, 402–414.
5 J. Chen, M. Q. Gu, Y. F. Zhou, D. J. Wan, Q. C. He, Y. H. Shi and Y. D. Liu, Efficient nitrate and perchlorate removal from aqueous solution via a novel electro-dialysis ion-exchange membrane bioreactor, *Chem. Eng. J.*, 2022, **430**, 132952.
6 J. Z. Qin, K. Wu, L. Z. Chen, X. T. Wang, Q. L. Zhao, B. J. Liu and Z. F. Ye, Achieving high selectivity for nitrate electrochemical reduction to ammonia over MOF-supported Ru_xO_y clusters, *J. Mater. Chem. A*, 2022, **10**, 3963–3969.
7 L. Jia, H. Xue, F. Xian, Y. Sugahara, N. Sakai, J. Nan, Y. Yamauchi, T. Sasaki and R. Z. Ma, Porous and partially dehydrogenated Fe^{2+}-containing iron oxyhydroxide nanosheets for efficient electrochemical nitrogen reduction reaction (ENRR), *Small*, 2023, **19**, 2303221.
8 Z. C. Zheng, D. Wu, L. Chen, S. Chen, H. Wan, G. Chen, N. Zhang, X. Liu and R. Z. Ma, Collaborative optimization of thermodynamic and kinetic for Ni-based hydroxides in electrocatalytic urea oxidation reaction, *Appl. Catal., B*, 2024, **340**, 123214.

9 F. B. Yao, M. C. Jia, Q. Yang, F. Chen, Y. Zhong, S. J. Chen, L. He, Z. J. Pi, K. J. Hou, D. B. Wang and X. M. Li, Highly selective electrochemical nitrate reduction using copper phosphide self-supported copper foam electrode: Performance, mechanism, and application, *Water Res.*, 2021, **193**, 116881.

10 S. J. Zuo, W. D. Xue, Y. Q. Zhang, J. Q. Chen and Z. Q. Lin, Atomically dispersed Fe motif-based electrocatalysts for hydrogen peroxide synthesis, *ChemNanoMat*, 2024, **10**, e202300476.

11 B. Wang, X. Zhu, X. D. Pei, W. G. Liu, Y. C. Leng, X. W. Yu, C. Wang, L. H. Hu, Q. M. Su, C. P. Wu, Y. F. Yao, Z. Q. Lin and Z. G. Zou, Room-Temperature laser planting of high-loading single-atom catalysts for high-efficiency electrocatalytic hydrogen evolution, *J. Am. Chem. Soc.*, 2023, **145**, 13788–13795.

12 L. Fang, S. Wang, C. Song, X. H. Yang, Y. K. Li and H. Liu, Enhanced nitrate reduction reaction via efficient intermediate nitrite conversion on tunable Cu_xNi_y/NC electrocatalysts, *J. Hazard. Mater.*, 2022, **421**, 126628.

13 S. J. Zuo, R. X. Guo, W. D. Xue, J. G. Shang, J. Q. Chen and Y. Q. Zhang, Decipher the key role of ketone toward singlet oxygen evolution in Fenton-like process for water decontamination, *Appl. Catal., B*, 2023, **339**, 123100.

14 R. D. Zhao, Q. Y. Yan, L. H. Yu, T. Yan, X. Y. Zhu, Z. Y. Zhao, L. Liu and J. Y. Xi, A Bi–Co corridor construction effectively improving the selectivity of electrocatalytic nitrate reduction toward ammonia by nearly 100%, *Adv. Mater.*, 2023, **35**, 2306633.

15 J. Martínez, A. Ortiz and I. Ortiz, State-of-the-art and perspectives of the catalytic and electrocatalytic reduction of aqueous nitrates, *Appl. Catal., B*, 2017, **207**, 42–59.

16 J. N. Gao, B. Jiang, C. C. Ni, Y. F. Qi, Y. Q. Zhang, N. Oturan and M. A. Oturan, Non-precious Co_3O_4-TiO_2/Ti cathode based electrocatalytic nitrate reduction: Preparation, performance and mechanism, *Appl. Catal., B*, 2019, **254**, 391–402.

17 S. Liang, M. Y. Zhang, G. M. Biesold, W. Choi, Y. J. He, Z. L. Li, D. F. Shen and Z. Q. Lin, Recent advances in synthesis, properties, and applications of metal halide perovskite nanocrystals/polymer nanocomposites, *Adv. Mater.*, 2021, **33**, 2005888.

18 S. Xu, A. Dong, Y. Hu, Z. Yang, S. Huang and J. Qian, Multidimensional MOF-derived carbon nanomaterials for multifunctional applications, *J. Mater. Chem. A*, 2023, **11**, 9721–9747.

19 L. Liu, S. Zheng, H. Chen, J. Cai and S. Zang, Tandem nitrate-to-ammonia conversion on atomically precise silver nanocluster/MXene electrocatalyst, *Angew. Chem., Int. Ed.*, 2024, **63**, e202316910.

20 L. Cheng, Ti. Ma, B. Zhang, L. Huang, W. Guo, F. Hu, H. Zhu, Z. Wang, T. Zheng, D. Yang, C. Siu, Q. Liu, Y. Ren, C. Xia, B. Z. Tang and R. Ye, Steering the topological defects in amorphous laser-induced graphene for direct nitrate-to-ammonia electroreduction, *ACS Catal.*, 2022, **12**, 11639–11650.

21 R. Hao, Y. Song, L. Yang, Y. Guo, X. Wu, Z. Ma, Z. Qian, F. Liu, Z. Wu and L. Wang, Electrochemical reduction of flue gas denitrification wastewater to ammonia using a dual-defective Cu_2O@Cu heterojunction electrode, *Environ. Sci. Technol.*, 2024, **58**, 5557–5566.

22 E. Murphy, Y. Liu, I. Matanovic, M. Rüscher, Y. Huang, A. Ly, S. Guo, W. Zang, X. Yan, A. Martini, J. Timoshenko, B. R. Cuenya, I. V. Zenyuk, X. Pan, E. D. Spoerke and P. Atanassov, Elucidating electrochemical nitrate and nitrite reduction over atomically-dispersed transition metal sites, *Nat. Commun.*, 2023, **14**, 4554.

23 Z. Liu, F. Shen, L. Shi, Q. Tong, M. Tang, Y. Li, M. Peng, Z. Jiao, Y. Jiang, L. Ao, W. Fu, X. Lv, G. Jiang and L. Hou, Electronic structure optimization and proton-transfer enhancement on titanium oxide-supported copper nanoparticles for enhanced nitrogen recycling from nitrate-contaminated water, *Environ. Sci. Technol.*, 2023, **57**, 10117–10126.

24 Y. Li, J. X. Ma, Z. C. Wu and Z. W. Wang, Direct electron transfer coordinated by oxygen vacancies boosts selective nitrate reduction to N_2 on a Co-CuO electroactive filter, *Environ. Sci. Technol.*, 2022, **56**, 8673–8681.

25 A. Baghdasaryan and T. Bürgi, Copper nanoclusters: designed synthesis, structural diversity, and multiplatform applications, *Nanoscale*, 2021, **13**, 6283–6340.

26 H. Wu, L. Huang, J. Timoshenko, K. Qi, W. Wang, J. Liu, Y. Zhang, S. Yang, E. Petit, V. Flaud, J. Li, C. Salameh, P. Miele, L. Lajaunie, B. Cuenya, D. Rao and D. Voiry, Selective and energy-efficient electrosynthesis of ethylene from CO_2 by tuning the valence of Cu catalysts through aryl diazonium functionalization, *Nat. Energy*, 2024, **9**, 422–433.

27 Y. L. Zhao, Y. Liu, Z. J. Zhang, Z. K. Mo, C. Y. Wang and S. Y. Gao, Flower-like open-structured polycrystalline copper with synergistic multi-crystal plane for efficient electrocatalytic reduction of nitrate to ammonia, *Nano Energy*, 2022, **97**, 107124.

28 G. A. Cerrón-Calle, A. S. Fajardo, C. M. Sánchez-Sánchez and S. Garcia-Segura, Highly reactive Cu-Pt bimetallic 3D-electrocatalyst for selective nitrate reduction to ammonia, *Appl. Catal., B*, 2022, **302**, 120844.

29 Y. T. Wang, W. Zhou, R. R. Jia, Y. F. Yu and B. Zhang, Unveiling the activity origin of a copper-based electrocatalyst for selective nitrate reduction to ammonia, *Angew. Chem., Int. Ed.*, 2020, **59**, 5350–5354.

30 Y. H. Wang, A. Xu, Z. Y. Wang, L. S. Huang, J. Li, F. W. Li, J. Wicks, M. C. Luo, D. H. Nam, C. S. Tan, Y. Ding, J. W. Wu, Y. W. Lum, C. T. Dinh, D. Sinton, G. F. Zheng and E. H. Sargent, Enhanced nitrate-to-ammonia activity on copper-nickel alloys via tuning of intermediate adsorption, *J. Am. Chem. Soc.*, 2020, **142**, 5702–5708.

31 J. F. Su, I. Ruzybayev, I. Shah and C. P. Huang, The electrochemical reduction of nitrate over micro-architectured metal electrodes with stainless steel scaffold, *Appl. Catal., B*, 2016, **180**, 199–209.

32 Q. G. Zhu, X. F. Sun, D. X. Yang, J. Ma, X. C. Kang, L. R. Zheng, J. Zhang, Z. H. Wu and B. X. Han, Carbon

dioxide electroreduction to C_2 products over copper-cuprous oxide derived from electrosynthesized copper complex, *Nat. Commun.*, 2019, **10**, 3851.

33 R. L. Hao, Y. C. Song, L. L. Yang, Y. X. Guo, X. H. Wu, Z. Ma, Z. Qian, F. Liu and L. D. Wang, Electrochemical reduction of flue gas denitrification wastewater to ammonia using a dual-defective Cu_2O@Cu heterojunction electrode, *Environ. Sci. Technol.*, 2024, **58**, 5557–5566.

34 A. R. Puigdollers, P. Schlexer, S. Tosoni and G. Pacchioni, Increasing oxide reducibility: The role of metal/oxide interfaces in the formation of oxygen vacancies, *ACS Catal.*, 2017, **7**, 6493–6513.

35 F. Cavalca, R. Ferragut, S. Aghion, A. Eilert, O. Diaz-Morales, C. Liu, A. L. Koh, T. W. Hansen, L. G. M. Pettersson and A. Nilsson, Nature and distribution of stable subsurface oxygen in copper electrodes during electrochemical CO_2 reduction, *J. Phys. Chem. C*, 2017, **121**, 25003–25009.

36 J. Zhao, Z. Shen, J. Yu, Y. Guo, M. A. Mushtaq, Y. B. Ding, Z. Q. Song, W. Zhang, X. Huang, Y. Li, D. Q. Liu and X. K. Cai, Constructing Cu-CuO heterostructured skin on Cu cubes to promote electrocatalytic ammonia production from nitrate wastewater, *J. Hazard. Mater.*, 2022, **439**, 129653.

37 Z. J. Zhang, Y. Liu, X. Z. Su, Z. W. Zhao, Z. K. Mo, C. Y. Wang, Y. L. Zhao, Y. Chen and S. Y. Gao, Electro-triggered joule heating method to synthesize single-phase CuNi nano-alloy catalyst for efficient electrocatalytic nitrate reduction toward ammonia, *Nano Res.*, 2023, **10**, 6632–6641.

38 J. F. Zhang, Y. Wang, Z. Y. Li, S. Xia, R. Cai, L. Ma, T. Y. Zhang, O. Ackley, S. Z. Yang, Y. C. Wu and J. J. Wu, Grain boundary-derived Cu^+/Cu^0 interfaces in CuO nanosheets for low overpotential carbon dioxide electroreduction to ethylene, *Adv. Sci.*, 2022, **9**, 2200454.

39 S. Ingavale, P. Marbaniang, M. Palabathuni, V. N. Kale and N. Mishra, Decoration of boron nanoparticles on a graphene sheet for ammonia production from nitrate, *Nanoscale*, 2023, **15**, 11497–11505.

40 X. D. Wen and J. Q. Guan, Recent advancement in the electrocatalytic synthesis of ammonia, *Nanoscale*, 2020, **12**, 8065–8094.

41 Y. Liu, J. W. Ma, S. L. Huang, S. Y. Niu and S. Y. Gao, Highly dispersed copper-iron nanoalloy enhanced electrocatalytic reduction coupled with plasma oxidation for ammonia synthesis from ubiquitous air and water, *Nano Energy*, 2023, **117**, 108840.

42 X. Y. Li, P. Deng, M. Q. Xu, Z. B. Peng, Y. H. Zhou, G. Jia, W. Wang, P. Gao and W. Wang, Multi-layer core-shell metal oxide/nitride/carbon and its high-rate electroreduction of nitrate to ammonia, *Nanoscale*, 2023, **15**, 14439–14447.

43 Y. T. Wang, C. H. Wang, M. Y. Li, Y. F. Yu and B. Zhang, Nitrate electroreduction: Mechanism insight, *in situ* characterization, performance evaluation, and challenges, *Chem. Soc. Rev.*, 2021, **50**, 6720–6733.

44 F. C. Lei, K. Li, M. Yang, J. Yu, M. M. Xu, Y. M. Zhang, J. F. Xie, P. Hao, G. W. Cui and B. Tang, Electrochemical reduction of nitrate on silver surface and an *in situ* Raman spectroscopy study, *Inorg. Chem. Front.*, 2022, **9**, 2734–2740.

45 Y. H. Wang, S. S. Zheng, W. M. Yang, R. Y. Zhou, Q. F. He, P. Radjenovic, J. C. Dong, S. N. Li, J. X. Zheng, Z. L. Yang, G. Attard, F. Pan, Z. Q. Tian and J. F. Li, In situ Raman spectroscopy reveals the structure and dissociation of interfacial water, *Nature*, 2021, **600**, 81–85.

46 J. J. Zhou, F. Pan, Q. F. Yao, Y. Q. Zhu, H. R. Ma, J. F. Niu and J. P. Xie, Achieving efficient and stable electrochemical nitrate removal by *in situ* reconstruction of Cu_2O/Cu electroactive nanocatalysts on Cu foam, *Appl. Catal., B*, 2022, **317**, 121811.

47 G. C. Halford and M. L. Personick, Bridging colloidal and electrochemical nanoparticle growth with in situ electrochemical measurements, *Acc. Chem. Res.*, 2023, **56**, 1228–1238.

48 H. X. Sun and Z. F. Hu, Electrochemical behavior of Al-1.5Mg-0.05Sn-0.01Ga alloy in KOH ethanol-water solutions for Al-Air battery, *J. Electrochem. Soc.*, 2019, **166**, A2477–A2484.

49 Y. Xu, Y. S. Wen, T. L. Ren, H. J. Yu, K. Deng, Z. Q. Wang, X. N. Li, L. Wang and H. J. Wang, Engineering the surface chemical microenvironment over CuO nanowire arrays by polyaniline modification for efficient ammonia electrosynthesis from nitrate, *Appl. Catal., B*, 2023, **320**, 121981.

50 Y. Zhang, M. Q. Xu, X. D. Xu, X. Y. Li, G. P. Zhu, G. Jia, B. C. Yang, R. L. Yin, P. Gao and W. Ye, Efficient interlayer confined nitrate reduction reaction and oxygen generation enabled by interlayer expansion, *Nanoscale*, 2022, **15**, 204–214.